energies

MDPI

Article

Effect of Blade Diameter on the Performance of Horizontal-Axis Ocean Current Turbine

Mansoor Ahmed Zaib [1], Arbaz Waqar [1], Shoukat Abbas [1], Saeed Badshah [1], Sajjad Ahmad [1,*], Muhammad Amjad [1], Seyed Saeid Rahimian Koloor [2] and Mohamed Eldessouki [2,3,4,*]

[1] Department of Mechanical Engineering, International Islamic University, Islamabad 44000, Pakistan; mansoor.bsme713@iiu.edu.pk (M.A.Z.); arbazwaqar0@gmail.com (A.W.); shoukatabbas1997@gmail.com (S.A.); saeed.badshah@iiu.edu.pk (S.B.); m.amjad@iiu.edu.pk (M.A.)
[2] Institute for Nanomaterials, Advanced Technologies and Innovation (CXI), Technical University of Liberec (TUL), Studentska 2, 461 17 Liberec, Czech Republic; s.s.r.koloor@gmail.com
[3] Empa, Swiss Federal Laboratories for Materials Science and Technology, Laboratory for Biomimetic, Membranes and Textiles, CH-9014 St. Gallen, Switzerland
[4] Faculty of Engineering, Mansoura University, Mansoura 35516, Egypt
* Correspondence: sa.ahmad@iiu.edu.pk (S.A.); mohamed.eldessouki@empa.ch (M.E.)

Abstract: The horizontal-axis ocean current turbine under investigation is a three-blade rotor that uses the flow of water to rotate its blade. The mechanical energy of a turbine is converted into electrical energy using a generator. The horizontal-axis ocean current turbine provides a nongrid robust and sustainable power source. In this study, the blade design is optimized to achieve higher efficiency, as the blade design of the hydrokinetic turbine has a considerable effect on its output efficiency. All the simulations of this turbine are performed on ANSYS software, based on the Reynolds Averaged Navier–Stokes (RANS) equations. Three-dimensional (CFD) simulations are then performed to evaluate the performance of the rotor at a steady state. To examine the turbine's efficiency, the inner diameter of the rotor is varied in all three cases. The attained result concludes that the highest C_m value is about 0.24 J at a tip-speed ratio (TSR) of 0.8 at a constant speed of 0.7 m/s. From 1 TSR onward, a further decrease occurs in the power coefficient. That point indicates the optimum velocity at which maximum power exists. The pressure contour shows that maximum dynamic pressure exists at the convex side of the advancing blade. The value obtained at that place is −348 Pa for case 1. When the dynamic pressure increases, the power also increases. The same trend is observed for case 2 and case 3, with the same value of optimum TSR = 0.8.

Keywords: horizontal-axis ocean current turbine; 3-blade design; coefficient of power and torque; CFD simulations

Citation: Ahmed Zaib, M.; Waqar, A.; Abbas, S.; Badshah, S.; Ahmad, S.; Amjad, M.; Rahimian Koloor, S.S.; Eldessouki, M. Effect of Blade Diameter on the Performance of Horizontal-Axis Ocean Current Turbine. *Energies* **2022**, *15*, 5323. https://doi.org/10.3390/en15155323

Academic Editor: Francesco Castellani

Received: 10 June 2022
Accepted: 18 July 2022
Published: 22 July 2022

1. Introduction

Overpopulation has led to an increased demand for resources such as energy, thus prompting developing nations to make engrossing traverse attempts to find alternative energy resources [1], as well as to look for environmentally friendly substitutes to fulfill our future needs [2,3]. Among various energy resources, ocean energy takes the lead, as it is predictable and reliable, enables big hoards, is easily built, has smooth maintenance, and is environmentally friendly [4,5]. These benefits have been intriguing and are progressing in the branch of force sustainability [6]. A thorough study analyzed the prospective and feasibility of both powerhouse storage-dependent and standalone sustainable off-grid water power applied sciences [7]. Water energy is attainable in various configurations, such as water tides, thermal energy, marine current, and osmotic pressure difference [8,9]. Sea streams are caused by blowing air, tidal current, osmotic pressure, salinity, and thermal gradient [10]. Energy from the ocean and marine currents is not only continuous but also reliable and globally present. The rapidly changing climate is affecting ocean current

and its circulating patterns. According to a study, since the 1900s, a 5% ocean current acceleration has been observed in the ocean at depths up to 2000 m [11]. This increase in ocean current acceleration shows considerable potential for obtaining kinetic energy from these high-speed currents. In recent years, the popularity of ocean current turbines made of light composite materials [12,13] has increased as these turbines are cheap, eco-friendly, and have significant potential in the future as countries such as China, the European Union, and Japan have shown keen interest in investing in these research fields [14]. HAOCT and VAOCT are two sub-divisions of OCT [15]. The world's primary business plate seaward flowing rotor "Seaflow" was a flat hub rotor comprising an estimated power of three hundred kilowatts and was presented by Marine Current Turbines Ltd. IT Power [16]. Since then, a large number of designs have been studied. After concluding the results, the HAOCT is the most preferred type due to its strong adroitness and large power output [17].

There are two types of horizontal-axis ocean current turbines—hub stream turbine and in-plane hub turbines [18]. The axial-flow turbines have a rotational axis aligned to the water current, and it works when water strikes the downstream side of the turbine and a lift force is produced on the blade that causes the rotation in the turbine. On the other hand, the in-plane turbine rotational axis and current flow are perpendicular, and thus, it operates due to the drag force that rotates its blades [19].

Chain studied the profile of the Savonius turbine, which works on the drag force. He changed the turbine profile to improve the rotor performance. The turbulence model k-epsilon was used for this operation [20]. Several different designs of OCT have been tested in the last few years to achieve optimum power from the flow. This research studied the idea and development of a rotor that acts on the flow at 2 mph. A water rotor was built based on their layout and form [21]. After studying different turbine rotor designs, the helical Savonius rotor consisting of the aspect and overlap ratio exhibited changes in the low torque coefficient. In a typical Savonius rotor, the negative static torque coefficient is almost 0. A detailed study of the rotor with a 90°-twist angle gave the best performance [22]. The turbine layout test in this examination was a drag-based HAOCT. This is organized as a low head hydrokinetic turbine for intercepting current energy, with a velocity as low as 0.4 m/s to more than 4.4 m/s [23]. The turbine works by the drag power on the turbine's concave blade side. As the current collides with the inside of the moving blade, a propelling force is formed, which causes drag power to force the rotor to turn. Its layout or design can be easily built, which removes the high cost incurred on the aerofoil blade designs of different horizontal and vertical turbines. For studying drag types of ocean turbines, a thorough examination was conducted to determine the efficiency of a deflector or protecting plates included in the general production enhancement of the turbine. Golecha et al. carried out an investigation on a Savonius turbine using a deflector plate and after removing that plate. The study revealed that the turbine with a plate increased the force coefficient by half more than that attained by a rotor without a plate [24]. Sahim et al. studied the Darrieus and a hybrid of Darrieus and Savonius turbines in relation to the deflector plate. The end product from the testing and survey depicted that the plate increased the force coefficient up to 30% for the Darrieus turbine and by 41% for the hybrid Darrieus [25]. A study performed for the hydrokinetic Savonius turbines depicted, in comparison with no plates, that a turbine using two protecting shield plates upstream at an absolute dot angle thickened the C_p of the turbine by 80% [26]. A higher-pressure differential ratio was achieved by a decrease in negative torque value on the blade. The ratio obtained between the approaching and returning blade led to a high torque and eventually higher power coefficient. The power coefficient was also enhanced by lowering the depth of the submersion of the turbine. The turbine's overall efficiency was also noted to increase [27].

The new concept of a turbine based on the drag mechanism has not been broadly studied. This work focused on the design variation of the rotor against the constant flow velocity. Three different rotor diameters were selected, and the optimal value of the rotor design for a higher value of efficiency is presented. For that purpose, a variation in the TSR was carried out for each case of rotor design. Numerical simulations were achieved with a range of TSR values from

0.6 m/s to 1.4 m/s. CFD software ANSYS was used to carry out the numerical simulation and the rotor was modeled in Solidworks software. The *k*-ε turbulence model was implemented for solving the Reynolds Average Navier–Stokes equation.

2. Theory

2.1. CFD Description

The Reynolds Average Navier–Stokes equation is used to solve the finite volume method. We subdivide the flow region into a Cartesian structured grid cycle. Every variable's average value is based on corresponding cells. A cell-centered value is used, omitting velocity. Each cell face is used to locate velocity. The CFD software Fluent was used for the current study. Fluent uses the numerical algorithm for the pressure velocity solver. For the pressure-based solver, it uses a combination of momentum and continuity equations to drive an equation of pressure. It is used because an efficient solution exists in an incompressible flow region [25,27].

The equation can be written concerning Cartesian coordinates x, y, and z components. In three-dimensional incompressible flows, the continuity equation in Fluent is given as:

$$C\frac{\partial \rho}{\partial t}+\frac{\partial}{\partial x}(uA_x)+\frac{\partial}{\partial y}(vA_y)+\frac{\partial}{\partial z}(wA_z)=\frac{R_{sor}}{\rho} \quad (1)$$

The momentum equation for all directions is:

$$\frac{\partial u}{\partial t}+1/C(uA_x\frac{\partial u}{\partial x}+vA_y\frac{\partial u}{\partial y}+wA_z\frac{\partial u}{\partial z})=-\frac{1}{\rho}\frac{\partial p}{\partial x}+G_x+f_x \quad (2)$$

$$\frac{\partial v}{\partial t}+1/C(uA_x\frac{\partial v}{\partial x}+vA_y\frac{\partial v}{\partial y}+wA_z\frac{\partial v}{\partial z})=-\frac{1}{\rho}\frac{\partial p}{\partial y}+G_y+f_y \quad (3)$$

$$\frac{\partial w}{\partial t}+1/C(uA_x\frac{\partial w}{\partial x}+vA_y\frac{\partial w}{\partial y}+wA_z\frac{\partial w}{\partial z})=-\frac{1}{\rho}\frac{\partial p}{\partial z}+G_z+f_z \quad (4)$$

In these equations, C is a constant that varies from 0 to 1. It depends on mesh cells; if a mesh cell occupies a fluid, then C is 1; otherwise, it is 0. (G_x, G_y, G_z) represents body acceleration and (f_x, f_y, f_z) represents the viscous acceleration in the respective direction (x, y, z). The velocity in the x, y, and z-direction is represented by u, v, and w, respectively, where A_x, A_y, and A_z show the area vector in the x, y, and z-directions, repectively. The density of the water is ρ, R_{sur} is the source term for density, and t is time.

2.2. Standard k-ε Turbulence Model

The characteristic flow for our simulation according to the condition is steady. The Y + value explains which turbulent model to use. Y + refers to the dimensionless distance parameter between the first node point of the cell to the wall. Our first layer thickness value is 1.91×10^{-3}. In this case, the Y + value is 30, which determines that the k-epsilon model is suitable.

Disparate to preliminary turbulence models, the *k*-ε turbulence model focuses on the technique that influences the turbulence kinetic energy. For high-Reynolds-number applications, it is better to use it under no-slip wall shear boundary conditions. However, Reynold shear stress is dominant in our case, so the *k*-ε turbulence model is used for numerical simulation. Numerous studies have explained that hydro and wind turbines by using the standard *k*-ε model have an admissible accordance with the results. Using the *k*-ε turbulence model, Sarmastudy conducted a numerical analysis of the Savonius water turbine and authenticated it with the performed results [28]. The value of the derived power coefficient was 0.390 from the achieved result and 0.4020 from the numerical results, manifesting an admissible divergence of 1.03% between the results. From an article published by Wahyudi in 2017, the comparison of horizontal-axis tidal turbines with deflectors and without deflectors was explained, showing a 2% efficiency increase [29].

Similarly, using the *k*-ε turbulence model in many numerical studies showed agreeable results in comparison with experimental values. Thus, these results prove the reliability of the *k*-ε turbulence model. The *k*-ε turbulence model can be derived from the incompressible Navier–Stokes equations. In this paper, the equation used in the model is described as:

For (*k*) turbulent kinetic energy:

$$\frac{\partial}{\partial t}(\rho k) + \frac{\partial}{\partial xi}(\rho k u_i) = \frac{\partial}{\partial_{xj}}\left[\left(\mu + \frac{\mu t}{\sigma k}\right)\frac{\partial k}{\partial_{xj}}\right] + N_k + N_b - \rho\varepsilon - D_M + S_k \quad (5)$$

For (ε) dissipation rate:

$$\frac{\partial}{\partial t}(\rho\varepsilon) + \frac{\partial}{\partial_{xi}}(\rho\varepsilon u_i) = \frac{\partial}{\partial xj}\left[\left(\mu + \frac{\mu t}{\sigma\varepsilon}\right)\frac{\partial\varepsilon}{\partial_{xj}}\right] + A1\varepsilon\frac{\varepsilon}{k}(Nk + A3\varepsilon Nb) - A2\varepsilon\rho\frac{\varepsilon^2}{k} + s\varepsilon \quad (6)$$

From the equations written above, we know that N_k is used to produce turbulent kinetic energy caused by the gradient velocity; N_b expresses the turbulent K.E, which results in the courtesy of buoyancy; D_M is the subsidy of fluctuating dilation to dissipation. x_i is the coordinate of the *i*th direction, μ is the viscosity, σk and $\sigma\varepsilon$ are the turbulent Prandtl numbers, $C\mu$ is a constant, and its value is 0.09. The value of $C\mu$ came from the number of iterations for a wide range of turbulent flows [21,29].

2.3. Performance of Equation

The following equations are then used to calculate the variables:

The equation for power for an ocean current turbine is given by

$$\mathrm{P_{avail}} = 0.5\rho A U^3 \quad (7)$$

In this formula ρ, A, and U represent the density of water, swept area of the turbine, and velocity of fluid, respectively.

The Reynolds number depends on the diameter of the rotor and is given by the formula:

$$\mathrm{Re} = \frac{\rho U D}{\mu} \quad (8)$$

where ρ, U, D, and μ represent the density of water, velocity, rotor diameter, and water viscosity, respectively. The formula for tip speed ratio is:

$$\mathrm{TSR} = \frac{\omega D}{2U} \quad (9)$$

where ω represents the angular velocity.

The torque coefficient is given by:

$$C_m = \frac{Q}{0.5 \times \rho \times As \times U^2 \times r} \quad (10)$$

where C_m represents the torque coefficient; Q is the torque extracted from the numerical simulation; A_s is the turbine's swept area, whose value is 0.665 m^2 ($A = H^*D$); r is the radius of the rotor.

The power coefficient is given by:

$$C_p = \frac{Q \times \omega}{0.5 \times \rho \times As \times U^3} \quad (11)$$

where C_p represents the power coefficient.

3. Numerical Setup

3.1. Geometry Modeling

Solidworks software was used to create geometry and was then exported to Ansys Fluent for numerical simulations. In this report, a horizontal-axis water turbine was investigated. The collation of this paper was carried out before the simulation, which explains the scheme we should use [waterotor]. The first step was to regenerate geometry, and Figure 1 shows the dimensions of case 1. The outer diameter of the turbine was 0.95 m. Therefore, the diameter of the inner arc was 0.34 m and the diameter of the outer arc was 0.68 m. The cylinder-like rotor had a radius of 0.175 m attached to the blade. The height of the turbine blade was 0.7 m. The end plate of radius 0.55 m was also attached with a turbine thickness of 0.05 m. Due to the difficulty and cost of computational time, the turbine's deflector and end plate effect will be examined in a future study. After this, the geometry was converted into a step file and was imported into DesignModeler for further explanation of the outer and inner domains. Figure 2 represents a 3D isometric view with end plates, and Figure 3 shows it without end plates.

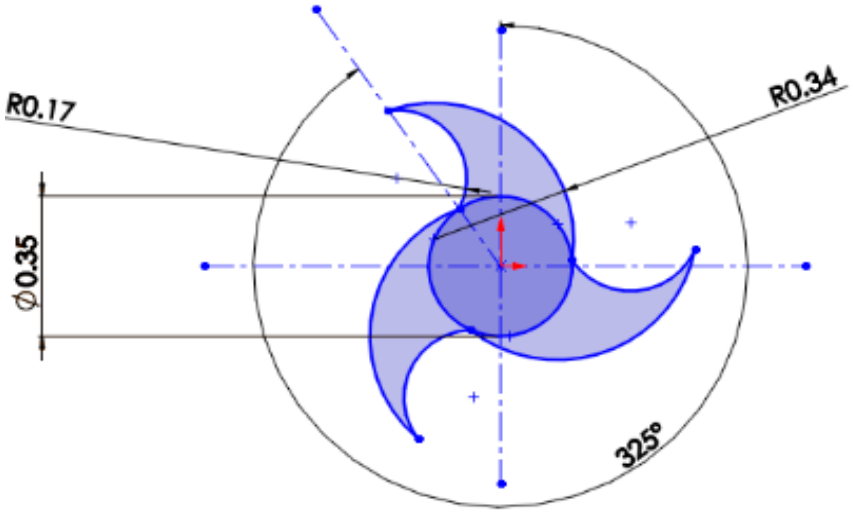

Figure 1. Dimensions of turbine (case 1).

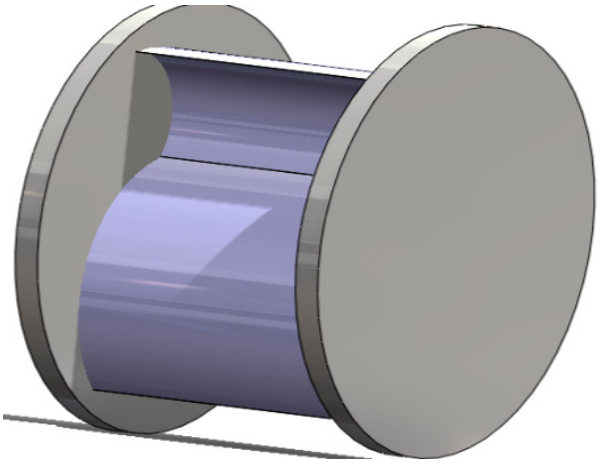

Figure 2. Isometric view of the turbine (case 1).

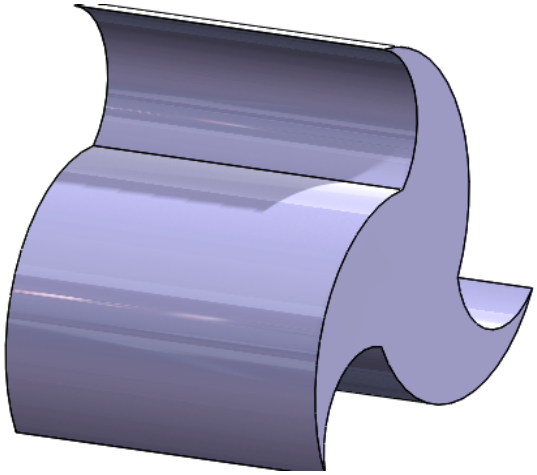

Figure 3. 3D view of turbine blade (case 1).

Figure 4 explains the dimensions for the outer domain, briefly explained as the distance from the global axis to the velocity inlet of 3.5 D (D is blade diameter). The distance from the pressure outlet to the rotor axis was 4.5 D. The side boundaries were at a distance of 0.5 from the turbine blade, which was considered a wall. The top and bottom boundaries were at a distance of 2D from the rotor axis, respectively. Water liquid was chosen from the cell zone as the fluid region. The standard *k*-ε turbulence model was selected in the viscosity and turbulence section. A no-slip condition was necessary for walls. For case 2 and case 3, the diameter of the inner rotor was 0.30 m and 0.40 m, respectively.

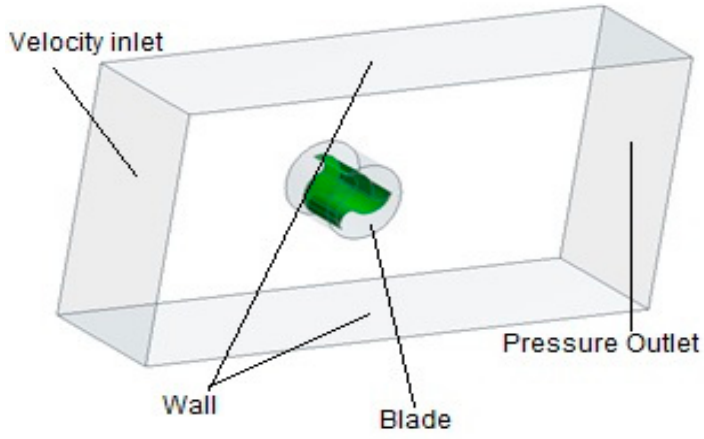

Figure 4. Isometric view of geometry with the outer domain.

3.2. Meshing

The meshing was performed in the package Fluent 20.1. Structured and unstructured meshing was carried out for the turbine. For the inner domain near the blade, unstructured grid spaces were taken. Body sizing was used for the blade mesh and the mesh size was divided into minimum and maximum according to the requirement. However, smaller and larger mesh sizes can be utilized to inspect if an additional decrease in mesh size is causing an error or deviation in the results. Due to the blade's sharp edge, the small mesh size helps the solver with better accuracy. However, different mesh sizes were used to check the accuracy and time constraint ratios. For the inner domain, a more refined mesh was used, while for the outer domain, a less refined mesh was used. Mesh independence analysis captured the C_m value for different refinement levels. The refinement level indicates a stable value as the mesh size decreases. Such a process has been practiced in advanced structures too [13,30].

From Table 1, we can see that at level 4, the results become mesh-independent. The level 3 (mesh cells = 1,164,860) case is selected for the study to optimize the computational cost. Thus, considering our computational cost refinement, level 3 is used for the study. Figure 5 shows the section view of geometry with unstructured grids. Figure 6 only represents the inner domain; the grid size is more refined in the inner domain. The inner domain has a smaller mesh cell size surrounding the blade geometry, and for the outer domain, a bigger mesh size would be used to achieve efficiency in computational time. Figure 7 shows the first layer thickness value we chose for our research. As for the scalable wall function, y+ should be greater than 11.225. Thus, the first layer thickness value is obtained from the y+ value and we use y+ = 50 in this paper.

Table 1. Mesh sensitivity of the flow domain.

Refinement Level	No of Mesh Cell	Torque
1	912,375	7.265479
2	1,097,000	8.768413
3	1,164,860	9.669196
4	1,456,978	9.671234

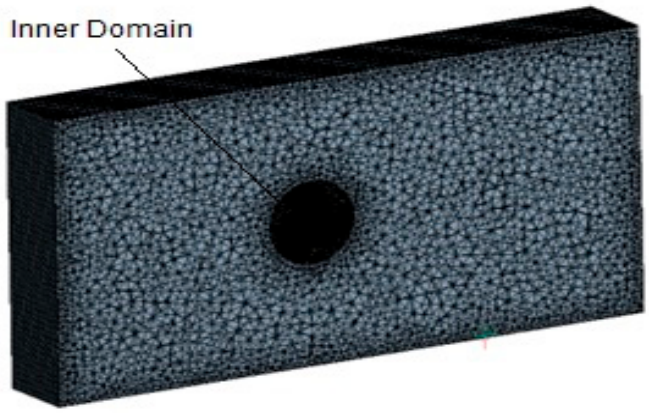

Figure 5. Sectional view of the geometry.

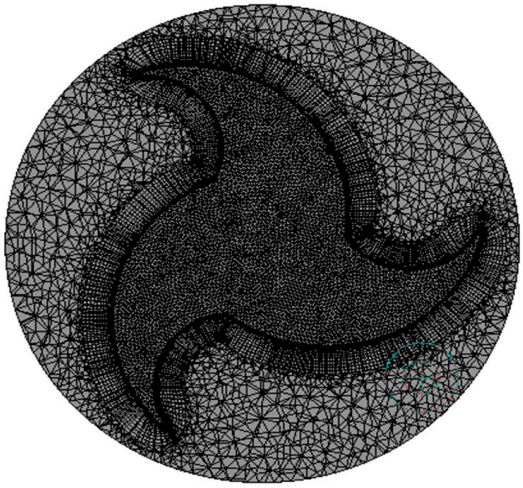

Figure 6. Meshing of the inner domain.

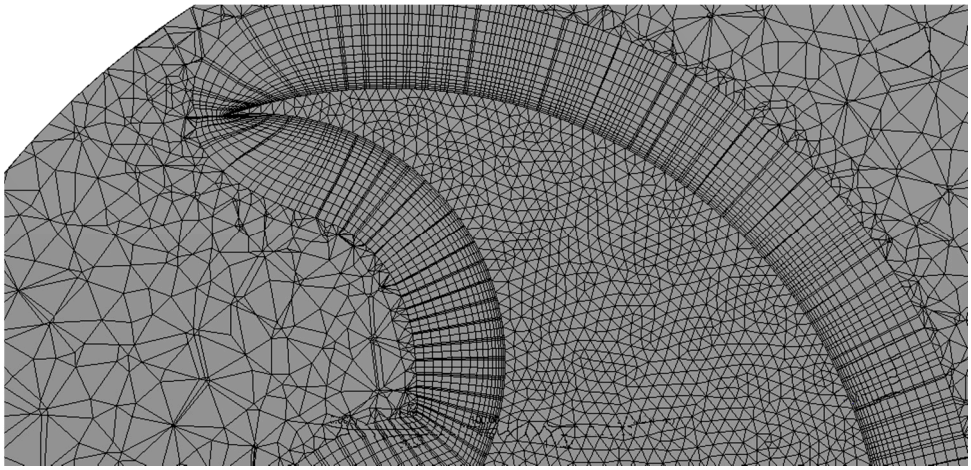

Figure 7. The thickness of the first blade layer.

4. Result and Discussion

4.1. Velocity and Pressure Contour

Velocity and pressure contours are achieved from CFD post-processing for three cases having different inner diameters. A numerical investigation is performed at 0.7 m/s at a different stage of the rotor. The tip speed ratio is performed at an interval of 0.6 to 1.2 at constant velocity. The torque value is obtained from the simulation. From the torque, C_p for each design can be calculated. As the pressure contour plot of all cases shows, the side static pressure decreases from upstream to the turbine downstream. The color scheme shows that pressure decreases from 331 Pa to −663 Pa for case 1 in Figure 8. For the remaining cases, the same trend is observed. At the downstream side of the blade, negative static pressure exists. The negative static pressure indicates a higher velocity. Higher velocity results in the rotation of the turbine. The same trend follows for Case 2 and Case 3, as shown in Figures 9 and 10, respectively.

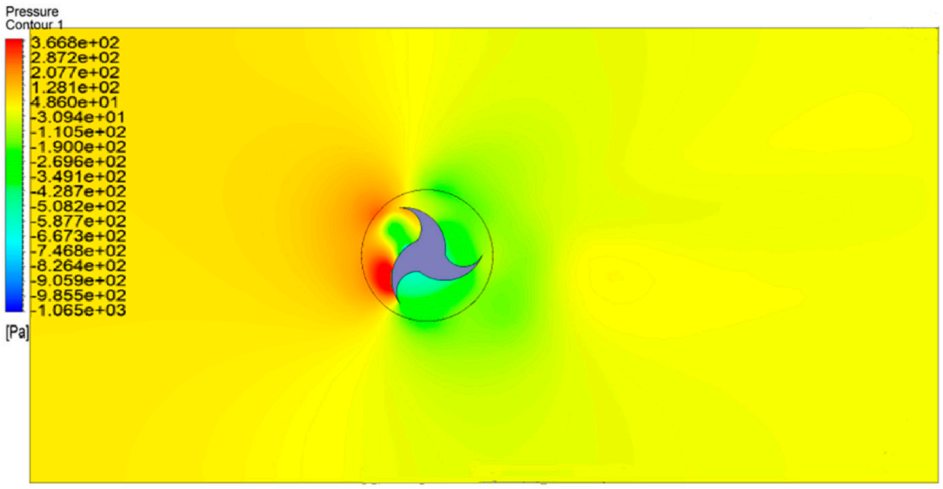

Figure 8. The pressure contour of Case 1 model.

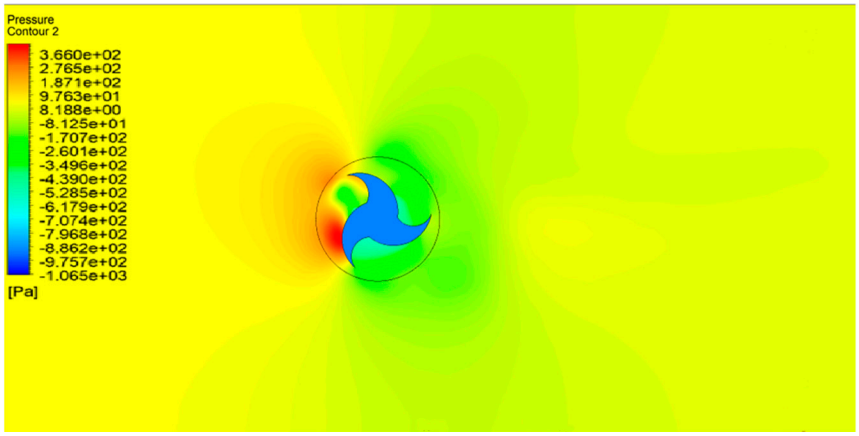

Figure 9. The pressure contour of Case 2 model.

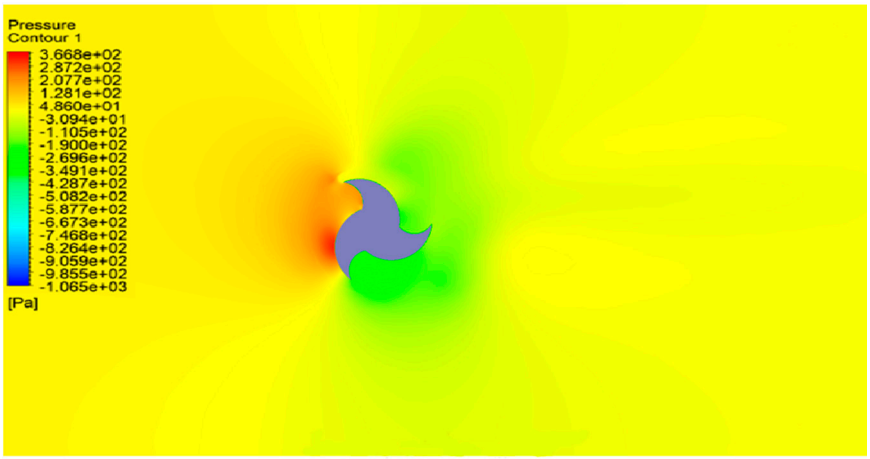

Figure 10. The pressure contour of Case 3 model.

Figure 10 shows that maximum dynamic pressure is at the downstream side of the blade. The value at that place obtained by the probe is −348 Pa for Case 1. As the dynamic pressure increases, the power increases.

For Case 1, in Figure 11, the velocity contour indicates that velocity at the upstream side of the blade decreases toward the downstream side of the blade. Thus, the velocity decreases from 0.65 to 0.5 m/s. This velocity difference produces rotation in the turbine. Figures 12 and 13 show the same trend of velocity distribution.

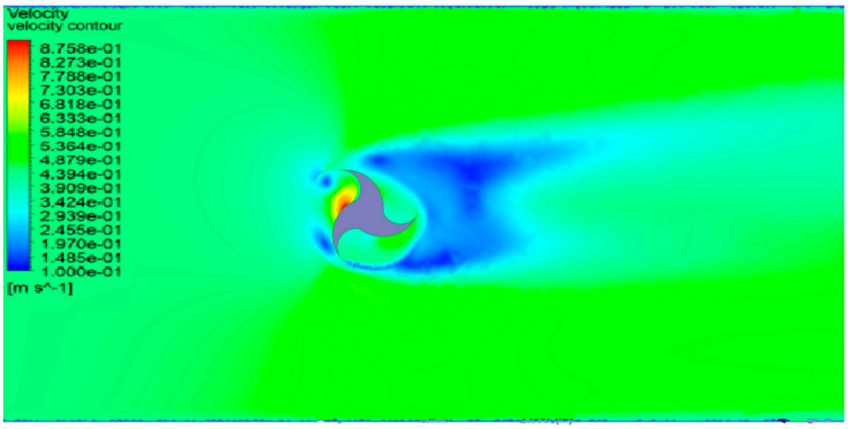

Figure 11. Velocity distribution of Case 1 model.

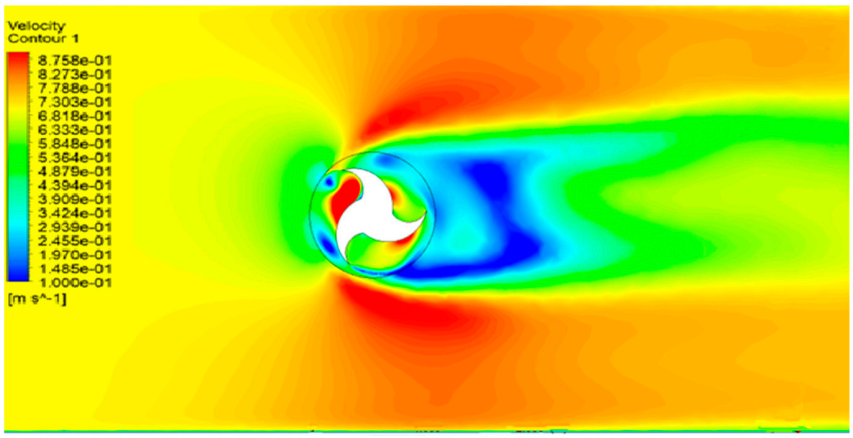

Figure 12. Velocity distribution of Case 2 model.

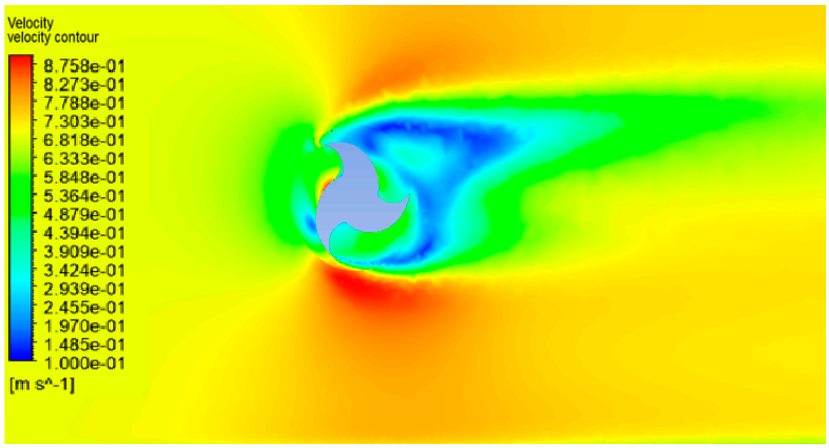

Figure 13. Velocity distribution of Case 3 model.

Therefore, with the increase in the intersection, the velocity magnitude difference on both sides of the turbine decreases gradually to ensure lift generation for the turbine. For all cases, the same trend follows.

4.2. Comparison of Torque and Power Curve

The performance equation is used for calculating the torque and power coefficients for all cases. Through formulation, we find the angular velocity at different tip speed ratios (0.6–1.2) at a constant velocity of 0.7 m/s. The findings are compared with published results [21]. We obtain the power coefficient after analysis. After validation, we change the inner diameter to improve the efficiency from the angular velocity, torque, and power coefficient for all cases, as shown in Tables 1 and 2.

Table 2. Values of Tip Speed Ratios (TSRs) and Angular Velocity at constant stream velocity.

Velocity (m/s)	Tip Speed Ratio (TSR)	Angular Velocity (Rad/s)
0.7	0.6	0.885
0.7	0.8	1.17
0.7	1	1.474
0.7	1.2	1.768

Figure 14 shows the relationship of iteration with torque values for case 1. After 278 iterations, a straight path is followed by the torque curve, due to which convergence

occurs with a residual target of 1×10^{-3}, and a maximum value of torque of 8.49 J is achieved for TSR 0.6. Torque is directly proportional to power. From the numerical values given in Table 3 and the plots in Figures 14 and 15, the highest value of C_m is achieved to be 0.225 J, 0.2 J, and 0.24 J, at a tip speed ratio of 1. From the results, it is clear that Case 3 has the highest C_m performance value. Hydrokinetic turbines are used due to the higher smoothness and stability compared to a wind turbine, but achieving an efficiency above 35% from the hydrokinetic turbine is difficult. For low heads, this type of turbine design should be used for ocean power with low heads that are less stressful. In a techno-economic analysis, using a hydrokinetic turbine independent of the river has not been of much economic benefit, but if one of the generators is responsible for synchronization or a hybrid system, it can be costly and profitable [21].

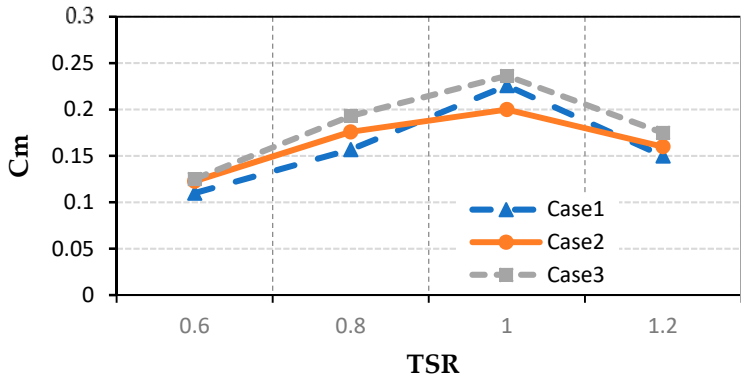

Figure 14. Variation in the torque coefficient against Tip Speed Ratio (TSR).

Table 3. Comparative values of C_m and C_p for different blade designs at different Tip Speed Ratios (TSRs).

Tip Speed Ratio	Case 1			Case 2			Case 3			Published Numerical Results [21]
	Torque	C_m	C_p	Torque	C_m	C_p	Torque	C_m	C_p	
0.6	8.4964	0.11	0.066	9.48659	0.1228	0.0736918	9.66793538	0.12516	0.0751	0.08
0.8	12.1227	0.15694	0.12556	13.5881	0.1759	0.1407367	14.9248751	0.19322	0.1545	0.17
1	17.4458	0.22586	0.225866	15.448	0.2	0.2	18.2490398	0.23626	0.23626	0.185
1.2	11.586	0.15	0.18	12.3584	0.16	0.192	13.517	0.175	0.21	0.17

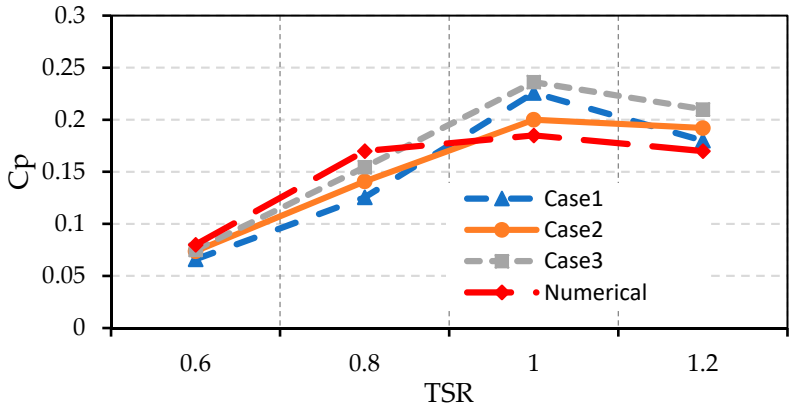

Figure 15. Variation in the power coefficient against Tip Speed Ratio (TSR) of different cases compared to the numerical data [21].

5. Conclusions

The three-dimensional numerical simulation is used to study the performance of a HOCT and compare the variation in inner diameter for all cases. The attained result

concludes that Case 3 shows the highest C_m value of about 0.24 J. The turbine is located at the center of the outer domain. Our study concludes that the tip speed ratio increases the power coefficient from 1 TSR, further decreasing the power coefficient. This point indicates an optimum velocity at which the maximum power exists. In the future, the increase in efficiency can be made possible by optimizing the aspect ratio. The present study only considers the variation in the inner diameter of the rotor. Future work will include the deflector and end plates of the blade. According to our research, the Savonius turbine improves with the deflector and end plates; however, the present turbine also operates on a similar drag mechanism.

Author Contributions: Conceptualization, M.A.Z., A.W., S.A. (Shoukat Abbas), S.B., S.A. (Sajjad Ahmad) and M.A.; Data curation, M.A.Z., A.W., S.B. and S.A. (Sajjad Ahmad); Formal analysis, M.A.Z., A.W., S.A. (Shoukat Abbas), S.B., S.A. (Sajjad Ahmad), M.A., S.S.R.K. and M.E.; Funding acquisition, S.S.R.K. and M.E.; Investigation, M.A.Z., S.B. and M.A.; Methodology, M.A.Z., A.W., S.A. (Shoukat Abbas), S.A. (Sajjad Ahmad), S.S.R.K. and M.E.; Project administration, S.A. (Sajjad Ahmad), S.S.R.K. and M.E.; Resources, S.S.R.K. and M.E.; Software, M.A.Z.; Supervision, S.A. (Sajjad Ahmad); Validation, M.A.Z., A.W., S.A. (Shoukat Abbas), S.B., M.A., S.S.R.K. and M.E.; Visualization, M.A.Z., A.W., S.B., M.A., S.S.R.K. and M.E.; Writing—original draft, M.A.Z., A.W. and S.A. (Shoukat Abbas); Writing—review & editing, A.W., S.A. (Shoukat Abbas), S.B., S.A. (Sajjad Ahmad), M.A., S.S.R.K. and M.E. All authors have read and agreed to the published version of the manuscript.

Funding: This research was partially funded by the European Union's Horizon 2020 research and innovation programme under the Marie Sklodowska-Curie grant agreement No 834966.

Acknowledgments: The authors acknowledge funding from the European Union's Horizon 2020 research and innovation programme under the Marie Sklodowska-Curie grant agreement No 834966.

Conflicts of Interest: The authors declare no conflict of interest.

Abbreviations and Symbols

CFD	Computational Fluid Dynamics
HAOCT	Horizontal-Axis Ocean Current Turbine
VAOCT	Vertical-Axis Ocean Current Turbine
OCT	Ocean Current Turbine
TSR	Tip Speed Ratio
N_k	Production term of turbulent kinetic energy because of the gradient of mean velocity
N_b	The turbulent kinetic energy due to buoyancy
DM	Contribution of fluctuating dilation to the all-inclusive dissipation rate
x_i	Coordinate in the ith direction
μ	Dynamic viscosity
μ_t	Turbulent dynamic viscosity
σ_k, σ_ε	Turbulent Prandtl numbers for 'k' and 'ε' respectively, have a value of 0.39.
A_x, A_y, A_z	Areas in the direction x, y, z, respectively
u, v, w	Velocities in the x, y, z-direction, respectively
$A1\varepsilon$, $A2\varepsilon$, $A3\varepsilon$	Model constants

References

1. Wellmann, J.; Morosuk, T. Renewable Energy Supply and Demand for the City of El Gouna, Egypt. *Sustainability* **2016**, *8*, 314. [CrossRef]
2. Flavio, R.; Arroyo, M.; Miguel, L. The Trends of the Energy Intensity and CO_2 Emissions Related to Final Energy Consumption in Ecuador: Scenarios of National and Worldwide Strategies. *Sustainability* **2020**, *12*, 20.
3. Saba, A.M.; Khan, A.H.; Akhtar, M.N.; Khan, N.A.; Koloor, S.S.R.; Petrů, M.; Radwan, N. Strength and flexural behavior of steel fiber and silica fume incorporated self-compacting concrete. *J. Mater. Res. Technol.* **2021**, *12*, 1380–1390. [CrossRef]
4. Bédard, R.; Jacobson, P.; Previsic, M.; Musial, W.; Varley, R. An Overview of Ocean Renewable Energy Technologies. *Oceanography* **2010**, *23*, 22–31. [CrossRef]
5. Alipour, R.; Alipour, R.; Koloor, S.S.R.; Petrů, M.; Ghazanfari, S.A. On the Performance of Small-Scale Horizontal Axis Tidal Current Turbines. Part 1: One Single Turbine. *Sustainability* **2020**, *12*, 5985. [CrossRef]

6. Nachtane, T.; Moumen, S. Design and Hydrodynamic Performance of a Horizontal Axis Hydrokinetic Turbine. *Int. J. Automot. Mech. Eng.* **2019**, *16*, 6453–6469. [CrossRef]
7. Lestari, H.; Arentsen, M.; Bressers, H.; Gunawan, B.; Iskandar, J. Parikesit Sustainability of Renewable Off-Grid Technology for Rural Electrification: A Comparative Study Using the IAD Framework. *Sustainability* **2018**, *10*, 4512. [CrossRef]
8. Magagna, D.; Uihlein, A. Ocean energy development in Europe: Current status and future perspectives. *Int. J. Mar. Energy* **2015**, *11*, 84–104. [CrossRef]
9. Alipour, R.; Alipout, R.; Fardian, F.; Kollor, S.; Petru, M. Performance improvement of a new proposed Savonius hydrokinetic turbine: A numerical investigation. *Energy Rep.* **2020**, *6*, 3051–3066. [CrossRef]
10. Le Traon, P.; Morrow, R. Ocean currents and eddies. In *International Geophysics*; Elsevier: Amsterdam, The Netherlands, 2001; pp. 171–215.
11. Hu, S.; Sprintall, J.; Guan, C.; McPhaden, M.; Wang, F.; Hu, D.; Cai, W. Deep-reaching acceleration of global mean ocean circulation over the past two decades. *Sci. Adv.* **2020**, *6*, eaax7727. [CrossRef]
12. Farokhi Nejad, A.; Alipour, R.; Shokri Rad, M.; Yazid Yahya, M.; Rahimian Koloor, S.S.; Petrů, M. Using Finite Element Approach for Crashworthiness Assessment of a Polymeric Auxetic Structure Subjected to the Axial Loading. *Polymers* **2020**, *12*, 1312. [CrossRef] [PubMed]
13. Kashyzadeh, K.; Koloor, S.R.; Bidgoli, M.O.; Petrů, M.; Asfarjani, A.A. An Optimum Fatigue Design of Polymer Composite-Compressed Natural Gas Tank Using Hybrid Finite Element-Response Surface Methods. *Polymers* **2021**, *13*, 483. [CrossRef] [PubMed]
14. Flajser, S.H.; Kash, D.E.; White, I.L.; Bergey, K.H.; Chartock, M.A.; Devine, M.D.; Salomon, S.N.; Young, H.W. Energy under the Oceans: A Technology Assessment of Outer Continental Shelf Oil and Gas Operations. *Technol. Cult.* **1975**, *16*, 122. [CrossRef]
15. Laws, N.D.; Epps, B.P. Hydrokinetic energy conversion: Technology, research, and outlook. *Renew. Sustain. Energy Rev.* **2016**, *57*, 1245–1259. [CrossRef]
16. Fraenkel, P.L. Marine current turbines: Pioneering the development of marine kinetic energy converters. *Proc. Inst. Mech. Eng. Part A J. Power Energy* **2007**, *221*, 159–169. [CrossRef]
17. Tian, W.; Mao, Z.; Ding, H. Design, test and numerical simulation of a low-speed horizontal axis hydrokinetic turbine. *Int. J. Nav. Arch. Ocean Eng.* **2018**, *10*, 782–793. [CrossRef]
18. Khan, M.; Bhuyan, G.; Iqbal, M.; Quaicoe, J. Hydrokinetic energy conversion systems and assessment of horizontal and vertical axis turbines for river and tidal applications: A technology status review. *Appl. Energy* **2009**, *86*, 1823–1835. [CrossRef]
19. Khan, M.; Iqbal, M.; Quaicoe, J. River current energy conversion systems: Progress, prospects and challenges. *Renew. Sustain. Energy Rev.* **2008**, *12*, 2177–2193. [CrossRef]
20. Chen, L.; Chen, J.; Zhang, Z. Review of the Savonius rotor's blade profile and its performance. *J. Renew. Sustain. Energy* **2018**, *10*, 013306. [CrossRef]
21. Maldar, N.R.; Ng, C.Y.; Ean, L.W.; Oguz, E.; Fitriadhy, A.; Kang, H.S. A Comparative Study on the Performance of a Horizontal Axis Ocean Current Turbine Considering Deflector and Operating Depths. *Sustainability* **2020**, *12*, 3333. [CrossRef]
22. Zakaria, A.; Ibrahim, M. Numerical Performance Evaluation of Savonius Rotors by Flow-driven and Sliding-mesh Approaches. *Int. J. Adv. Trends Comput. Sci. Eng.* **2019**, *8*, 57–61.
23. Asterita, T.J. Available online: www.waterotor.com (accessed on 20 December 2021).
24. Golecha, K.; Eldho, T.; Prabhu, S. Influence of the deflector plate on the performance of modified Savonius water turbine. *Appl. Energy* **2011**, *88*, 3207–3217. [CrossRef]
25. Sahim, K.; Ihtisan, K.; Santoso, D.; Sipahutar, R. Experimental Study of Darrieus-Savonius Water Turbine with Deflector: Effect of Deflector on the Performance. *Int. J. Rotating Mach.* **2014**, *2014*, 203108. [CrossRef]
26. Hemida, M.; Abdel-Fadeel, W.A.; Ramadan, A.; Aissa, W. Numerical Investigation of hydrokinetic Savonius rotor with two shielding plates. *Appl. Model. Simul.* **2019**, *3*, 85–94.
27. Kolekar, N.; Banerjee, A. Performance characterization and placement of a marine hydrokinetic turbine in a tidal channel under boundary proximity and blockage effects. *Appl. Energy* **2015**, *148*, 121–133. [CrossRef]
28. Sarma, N.; Biswas, A.; Misra, R. Experimental and computational evaluation of Savonius hydrokinetic turbine for low velocity condition with comparison to Savonius wind turbine at the same input power. *Energy Convers. Manag.* **2014**, *83*, 88–98. [CrossRef]
29. Wahyudi, B.; Adiwidodo, S. The influence of moving deflector angle to positive torque on the hydrokinetic cross flow savonius vertical axis turbine. *Int. Energy J.* **2017**, *17*, 11–22.
30. Koloor, S.S.R.; Karimzadeh, A.; Tamin, M.N.; Shukor, M.H.A. Effects of Sample and Indenter Configurations of Nanoindentation Experiment on the Mechanical Behavior and Properties of Ductile Materials. *Metals* **2018**, *8*, 421. [CrossRef]